# Micropillar compression deformation of single crystals of Fe$_3$Ge with the L1$_2$ structure

Zhenghao Chen [a,*], Haruyuki Inui [a,b]

[a] Center for Elements Strategy Initiative for Structural Materials (ESISM), Kyoto University, Sakyo-ku, Kyoto 606-8501, Japan
[b] Department of Materials Science and Engineering, Kyoto University, Sakyo-ku, Kyoto 606-8501, Japan

### ARTICLE INFO

### ABSTRACT

The plastic deformation behavior of single crystals of Fe$_3$Ge with the L1$_2$ structure has been investigated at room temperature as a function of crystal orientation by micropillar compression tests. In addition to slip on (010), slip on (111) is observed to occur in Fe$_3$Ge for the first time. The CRSS (critical resolved shear stress) for (111)[10$\bar{1}$] slip, estimated by extrapolating the size-dependent strength variation to the 'bulk' size, is ~240 MPa, which is almost 6 times that (~40 MPa) for (010)[10$\bar{1}$] slip similarly estimated. The dissociation scheme for the superlattice dislocation with $\boldsymbol{b}$=[10$\bar{1}$] is confirmed to be of the APB (anti-phase boundary)-type both on (010) and on (111), in contrast to the previous prediction for the SISF (superlattice intrinsic stacking fault) scheme on (111) because of the expected APB instability. While superlattice dislocations do not have any preferential directions to align when gliding on (010) (indicative of low frictional stress at room temperature), the alignment of superlattice dislocations along their screw orientation is observed when gliding on (111). This is proved to be due to thermally-activated cross-slip to form Kear-Wilsdorf locks, indicative of the occurrence of yield stress anomaly that is observed in many other L1$_2$ compounds such as Ni$_3$Al. Some important deformation characteristics expected to occur in Fe$_3$Ge (such as the absence of SISF-couple dissociation and the occurrence of yield stress anomaly) will be discussed in the light of the experimental results obtained (APB energies on (111) and (010) and CRSS values for slip on (111) and (010)).

## 1. Introduction

Many intermetallic compounds with the L1$_2$ structure such as Ni$_3$Al have been known to exhibit the 'yield stress anomaly' (YSA), in which the yield stress increases with the increase in temperature. Because of the technological importance of this phenomenon when these L1$_2$ compounds are used as the strengthening phase of $\gamma$ (FCC: face-centered cubic)/$\gamma$' (L1$_2$) two-phase Ni-based superalloys for high-temperature applications [1,2], the phenomenon has been the subject of extensive scientific studies for decades [3,4]. There is a general agreement that the yield stress anomaly occurs as a result of thermally-activated cross-slip of the superlattice dislocation with $\boldsymbol{b}$ (Burgers vector)=[10$\bar{1}$] dissociated into the APB (anti-phase boundary)-scheme (shown below as (1)) from (111) octahedral to (010) cube slip planes [3,4].

$$\left[10\bar{1}\right] \rightarrow 1/2\left[10\bar{1}\right] + (APB) + 1/2\left[10\bar{1}\right] \qquad (1)$$
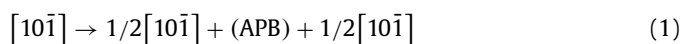
In L1$_2$ compounds in which the APB fault is stable on (111), thermally-activated cross-slip of the superpartial dislocation with $\boldsymbol{b}$ = 1/2[10$\bar{1}$] is believed to occur with the driving force arising from the difference in the APB energies on (111) and (010) as well as the torque force acting between a screw superpartial pair [3,4], and generally to result in the formation of Kear-Wilsdorf locks where the APB fault between two-coupled superpartials is mostly on (010) instead of the (111) slip plane [3].

However, all L1$_2$ compounds do not necessarily behave similarly to exhibit YSA [5,6]. In particular, Pt$_3$Al and Fe$_3$Ge are frequently counted as typical exceptions for this. The reason for this has usually been described to be instability of the APB fault on (111) [3,5-9]. In these L1$_2$ compounds, the APB fault on (111) is unstable or of very high energy, and the APB dissociation scheme of the superlattice dislocation with $\boldsymbol{b}$=[10$\bar{1}$] according to (1) cannot occur. Instead, another dissociation scheme called the SISF (superlattice intrinsic stacking fault) scheme (shown below as (2)) is believed to occur on (111) for these L1$_2$ compounds [7-9].
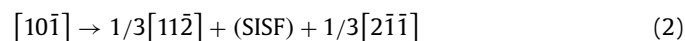
$$\left[10\bar{1}\right] \rightarrow 1/3\left[11\bar{2}\right] + (SISF) + 1/3\left[2\bar{1}\bar{1}\right] \qquad (2)$$

The occurrence of YSA is not expected with the dislocation dissociated according to the SISF scheme, accounting for the observed different deformation behavior for these exceptional $L1_2$ compounds. More importantly, slip in these $L1_2$ compounds is known to occur more easily on (010) than on (111). This has been explained in terms of the very high Peierls stress for the motion of the super-Shockley partial dislocation with $\boldsymbol{b} = 1/3[11\bar{2}]$, arising from its non-planar core structure [4]. Indeed, the CRSS (critical resolved shear stress) values are reported to be lower for slip on (001) than slip on (111) in $Pt_3Al$ [5,6,10]. Recently, however, the dissociation scheme for the superlattice dislocation in $Pt_3Al$ is proved to be of the APB-scheme but not of the SISF scheme [11,12]. This clearly indicates that the APB instability cannot account for the absence of the APB-scheme dissociation of the superlattice dislocation and, hence the absence of YSA, at least, in $Pt_3Al$. While detailed studies have been made for $Pt_3Al$ with the use of single crystals [11,12], similar studies are considered to be difficult to make for $Fe_3Ge$ because there is practically no possibility to produce single crystals due to the limitation from the corresponding phase diagram. All previous studies on $Fe_3Ge$, therefore, used polycrystals and found that slip occurs on (001) exhibiting a normal temperature dependence of yield stress [13-17]. Although the absence of slip on (111) in $Fe_3Ge$ has been discussed in terms of the APB instability, this is questionable when referring to the recent results in $Pt_3Al$ [11,12]. The absence of slip on (111) in $Fe_3Ge$ must be due to the fact that the CRSS value is lower for slip on (010) than for slip on (111), but this has yet to be experimentally proved with the use of single crystals. Although 'bulk' single crystal growth is impossible for $Fe_3Ge$, we can employ Focused Ion Beam (FIB) machining to produce oriented single crystals of the micronmeter size (often called micropillar specimens) even from a 'bulk' polycrystal so as to evaluate their mechanical properties in compression with a nano-indenter equipped with a flat punch [18,19]. We have successfully deduced the operative slip systems and their CRSS values in a number of materials with micropillar compression tests [20-30].

In the present study, we investigate the room-temperature deformation behavior of single crystals of $Fe_3Ge$ with the $L1_2$ structure at room temperature as a function of crystal orientation with the use of small-scale specimens in the micropillar form cut out from polycrystals by FIB machining, in order to see if slip on {111} occurs in $Fe_3Ge$. We then discuss factors controlling the occurrence of either slip on {111} or slip {010} as well as the expected mechanical properties carried by slip on {111} in $Fe_3Ge$.

## 2. Experimental procedures

Ingots with a nominal composition of Fe-25 at.% Ge were prepared by arc-melting high-purity Fe and Ge in a proper ratio under an Ar gas flow. The ingots were annealed at 1273 K for 1 week for homogenization, then at 873 K for 2 months for the $L1_2$-phase formation, followed by water quenching. Then, specimen surfaces were mechanically polished and finished with diamond paste to mirror finish, followed by electropolishing ($HClO_4$:1-$C_4H_7OH$:$CH_3OH = 1$:6:12, 18 V, 233 K) prior to focused ion beam (FIB) machining. Micropillar specimens with a square cross section having an edge length $L$ ranging from 1 to 10 $\mu$m and an aspect ratio of about 1:2.5 were cut from the oriented specimens with our JEOL FIB-4000 system (with 30 kV Ga+ ions). Three compression-axis orientations, $[\bar{1}, 1, 15]$, $[\bar{1}13]$ and $[\bar{5}68]$ were selected, as shown in Fig. 1. The Schmid factors for possible $(111)[10\bar{1}]$ and $(010)[10\bar{1}]$ slip systems are listed in Tables 1 for each loading axis orientation, together with the N value (the Schmid factor ratio for these two slip systems). The propensity for the occurrence of $(111)[10\bar{1}]$ slip is expected to increase with the decrease in the N value. Micropillar specimens were deformed
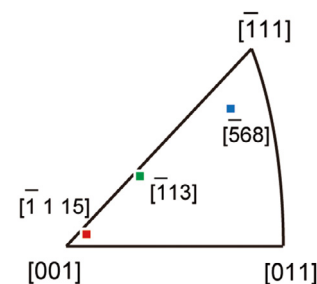


**Fig. 1.** Stereographic projection of compression-axis orientations investigated.

in compression using an Agilent Technologies Nano Indenter G200 nanomechanical tester equipped with a flat-punch diamond tip at room temperature under the displacement-rate-controlled mode at a nominal strain rate of $1 \times 10^{-4}$ /s. Microstructures of micropillar specimens before and after compression tests were examined by scanning electron microscopy (SEM) with a JEOL JSM-7001FA electron microscope. Deformation microstructures developed in the deformed micropillars were investigated by transmission electron microscopy (TEM) with a JEOL JEM-2000FX electron microscope operated at 200 kV. Specimens for TEM observations were prepared by FIB-SEM in-situ lift-out technique using a FEI Quanta 3D 200i Dual-Beam system equipped with an Omniprobe nanomanipulator. Thin foil specimens for TEM analysis were cut out parallel to the observed slip plane (either (111) or (010)) as much as possible.

## 3. Results

### 3.1. Microstructure prior to deformation

The alloy after prolonged (for 2 months) annealing at 873 K exhibits essentially a $L1_2$ single-phase microstructure with a grain size of a few hundred $\mu$m, except for sporadically occurring second-phase particles of presumably $\eta$-$Fe_2Ge$ (when judged from the chemical composition (Fe-37 at.% Ge) by EDS analysis in the SEM). However, stacking faults that had formed on {111} planes during the $D0_{19}$ to $L1_2$ phase transformation could not be completely eliminated as observed in previous studies [15,31,32], since the crystal structures of these two phases differ from each other only in the stacking sequence of the hexagonally-arranged $Fe_3Ge$ stoichiometric atomic layers; the ABC and AB stackings for the cubic $L1_2$ and hexagonal $D0_{19}$ phases, respectively, similarly as for FCC (face-centered cubic) and HCP (hexagonal close-packed) structures. The distribution of these {111} stacking faults are very heterogeneous (Fig. 2). They are formed generally on multiple {111} planes, and while they are formed very densely in some areas and these areas are often separated from each other at a distance ranging from 0.3 to 1 $\mu$m. This means that some {111} stacking faults with varying densities are inevitably contained in micropillar specimens tested.

### 3.2. Deformation behavior of $[\bar{1}13]$- and $[\bar{5}68]$-oriented crystals

#### 3.2.1. Stress-strain behavior

Typical stress-strain curves obtained for $[\bar{1}13]$- and $[\bar{5}68]$-oriented crystals with various specimen sizes are shown in Figs. 3(a) and (b), respectively. The tests in Figs. 3(a) and (b) were all interrupted immediately after recognition of yielding for the ease of slip trace analysis. In contrast to what is observed in bulk polycrystals where failure occurs soon after yielding by cracking along the grain boundary [15,17], failure does not usually occur even deformation continues above a plastic strain level of 5% in micropillar compression deformation. For both orientations, the
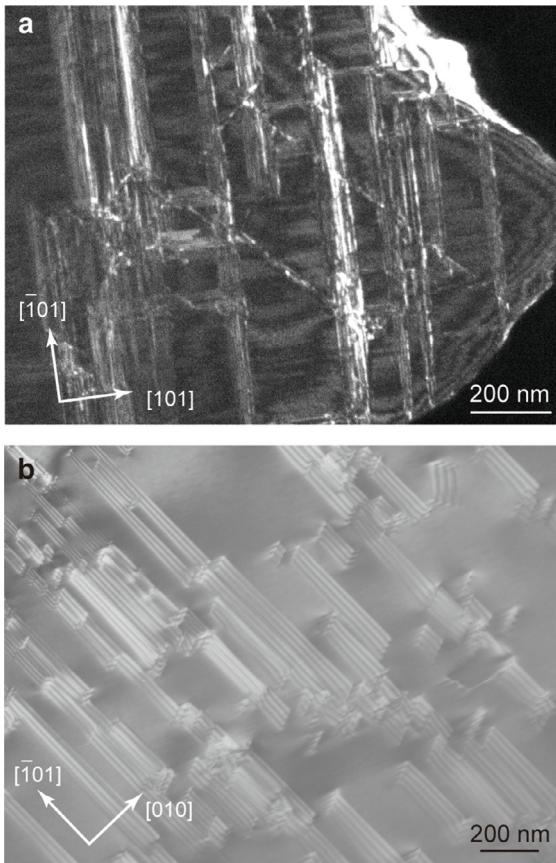
**Fig. 2.** TEM microstructures of Fe$_3$Ge prior to micropillar deformation. The electron beam incidents for (a) and (b) are respectively near [010] and [101].
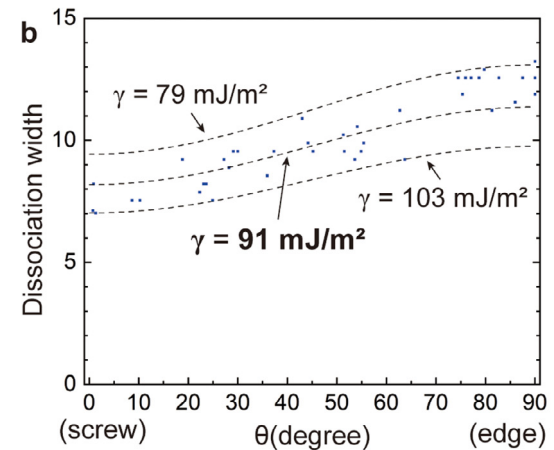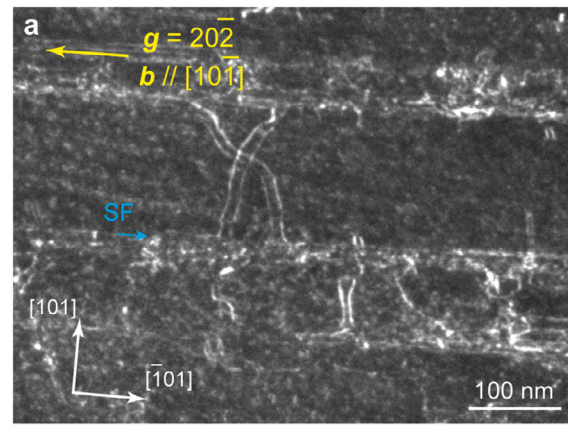


**Fig. 4.** Weak-beam dark-field TEM image of a typical deformation microstructure carried by slip on (010) in a [$\overline{5}$68]-orientated crystal. The thin foil was cut parallel to the (010) slip plane. .

yield stress defined as the stress at which the first strain burst occurs tends to decrease with the increase in specimen size (edge length L), as observed in many other metallic materials [20-30].

Deformation markings observed for [$\overline{1}$13]- and [$\overline{5}$68]-oriented crystals with the specimen sizes (L) of 4.2 and 6.1 $\mu$m are shown in Figs. 3(c) and (d), respectively. The deformation marking observed are those corresponding to slip on (010). Deformation markings corresponding to slip on (010) are consistently observed for all [$\overline{1}$13]- and [$\overline{5}$68]-oriented crystals tested, regardless of specimen size. This is consistent with our expectation for the occurrence of (010)[10$\overline{1}$] slip from the higher N values for these two orientations

*3.2.2. Dislocation structures for slip on (010)*

Fig. 4(a) shows a typical dislocation structures carried by slip on (010) in a [$\overline{5}$68]-oriented crystal. The thin foil for TEM observations was cut parallel to the (010) slip plane. Many striations running horizontally in the image (as marked SF) correspond to stacking faults on ($\overline{1}\overline{1}$1) that exist prior to micropillar deformation. Some dislocations with **b** (Burgers vector) =[10$\overline{1}$] are observed to bow out on (010) between closely spaced stacking faults. These dislocations are obviously dissociated into two partial dislocations with **b** = 1/2[10$\overline{1}$] separated by APB when judged from the fact that both of the partial pair are simultaneously out of contrast when imaged with **g** (reflection vector) =202 as well as that the contrast of the two partials are reversed upon the reflection vector reversal (not shown in Fig. 4). The dissociation widths measured are typically 7.7 ± 0.6 and 12.5 ± 0.6 nm for pure screw and edge segments, respectively, as shown in Fig. 4(b). With the elastic con-
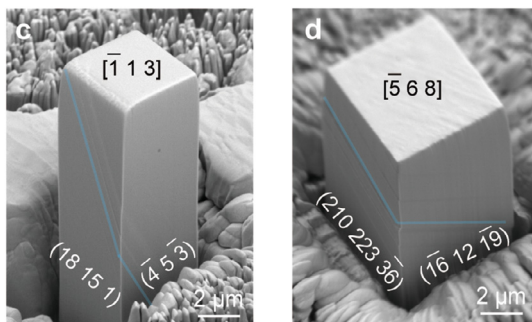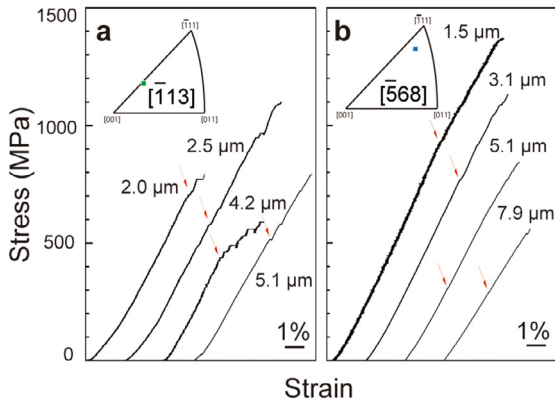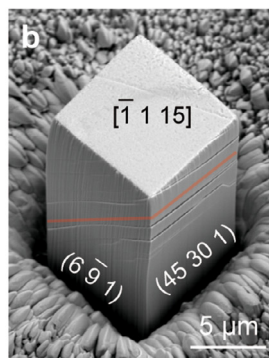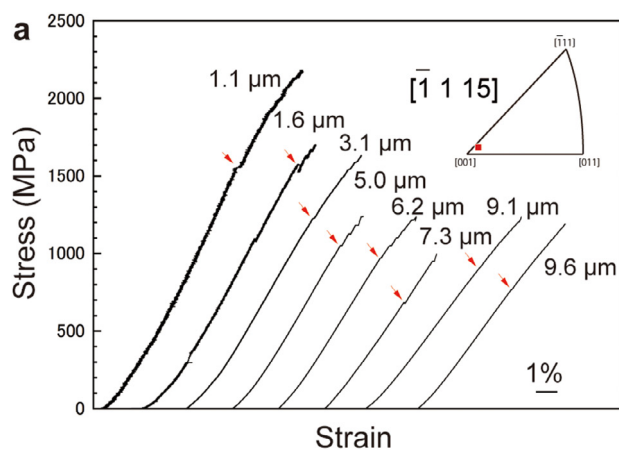


**Fig. 3.** (a,b) Selected stress-strain curves and (c,d) typical micropillar single crystal specimens after deformation for (a,c) [$\overline{1}$13]- and (b,d) [$\overline{5}$68]-orientated crystals.

**Fig. 5.** (a) Selected stress-strain curves and (b) typical micropillar single crystal specimen after deformation for $[\bar{1}, 1, 15]$-orientated crystals.
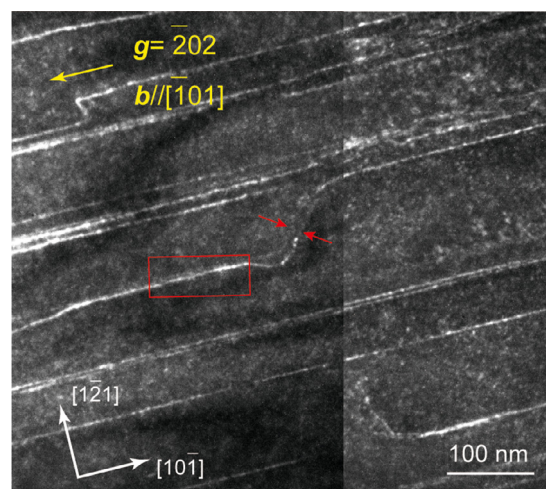


**Fig. 6.** Weak-beam dark-field TEM image of a typical deformation microstructure carried by slip on (111) in a $[\bar{1}, 1, 15]$-orientated crystal. The thin foil was cut parallel to the (111) slip plane.

stants (shear modulus $G = 74.0$ GPa and Poisson ratio $\nu=0.280$) given by Balk et al. [13], the APB energy on (010) is consistently calculated with isotropic elasticity theory to be $91\pm12$ mJ/m$^2$, being consistent with the previous reports [7,9,13].

These dislocations gliding on (010) seem not to align along any particular crystallographic directions (although the dislocations need inevitably interact with pre-existing $(\bar{1}11)$ stacking faults along their screw orientation), indicating a rather low Peierls stress for their motion at room temperature. This is consistent with what was observed previously for slip on (010) in Fe$_3$Ge with the L1$_2$ structure by others [13-15].

### 3.3. Deformation behavior of $[\bar{1}, 1, 15]$-oriented crystals

#### 3.3.1. Stress-strain behavior

Typical stress-strain curves obtained for $[\bar{1}, 1, 15]$-orientated crystals with various specimen sizes are shown in Fig. 5(a). The tests in Fig. 5(a) were all interrupted immediately after recognition of yielding for the ease of slip trace analysis. For this orientation, the yield stress defined as the stress at which first strain burst occurs tends to decrease with the increase in specimen size (edge length $L$), as in the case of $[\bar{1}13]$- and $[\bar{5}68]$-oriented crystals.

Deformation markings observed for $[\bar{1}, 1, 15]$-orientated crystals with the specimen sizes ($L$) of 8.0 $\mu$m are shown in Fig. 5(b). The deformation markings observed are those corresponding to slip on (111) that is the most highly stressed plane among four {111} planes. Deformation markings corresponding to slip on (111) are exclusively observed for all $[\bar{1}, 1, 15]$-orientated crystals tested, regardless of specimen size. This is the first observation of the operation of slip on {111} octahedral planes in Fe$_3$Ge, in which slip on {010} has been reported to be only the operative slip system [13-

15,17], being consistent with our expectation for the occurrence of $(111)[10\bar{1}]$ slip from the lower N value for the $[\bar{1}, 1, 15]$ orientation.

#### 3.3.2. Dislocation structures for slip on (111)

Fig. 6 shows a typical dislocation structure observed in a $[\bar{1}, 1, 15]$-orientated crystal deformed at room temperature. The TEM thin foil was cut parallel to the (111) slip plane. Contrast analysis indicates that the Burgers vector of most dislocations imaged is $[10\bar{1}]$. Straight screw dislocations dissociated into two-coupled partials are observed to be connected with a kink with an edge component. Weak-beam contrast analysis made in the framed area of Fig. 6 indicates that each of these two-coupled partials has $\boldsymbol{b} = 1/2[10\bar{1}]$ separated by an APB, since the contrast of the two-coupled partials are reversed upon reversal of the reflection vectors (Figs. 7(a) and (b)) and they are simultaneously invisible when imaged with $\boldsymbol{g} = 1\bar{1}1$ (Fig. 7(c)). This is a clear indication that slip on (111) in Fe$_3$Ge is carried by superlattice dislocations dissociated into the APB scheme but not by those dissociated into the SISF scheme. The dissociation of the two-coupled-superpartials along the kink portion (called superkink) in Fig. 6 must be on the (111) slip plane. Then, the APB energy on (111) ($\gamma_{APB}^{(111)}$) can be estimated to be $99\pm9$ mJ/m$^2$ from the measured dissociation width ($9.2 \pm 0.8$ nm) along a segment about 40$°$ away from the pure edge segment (indicated by arrows in Fig. 6). This is the first experimental evaluation of the APB energy on (111) in Fe$_3$Ge. On the other hand, the dissociation plane for the screw segments can be either on (111) or on (010), depending on whether cube cross-slip to form a Kear-Wilsdorf lock had occurred or not. Tilting experiments made about the Burgers vector direction ($[10\bar{1}]$) in Fig. 7 indicates that the dissociation of the APB-coupled screw super-partials occurs mostly on (010) since the projected dissociation distance is the widest when imaged along the [010] direction (Fig. 7(e)). This is a clear indication of the formation of the Kear-Wilsdorf lock during the motion of APB-coupled super-partial dislocations at room temperature in Fe$_3$Ge. The APB energy on (010) ($\gamma_{APB}^{(010)}$) is estimated from the dissociation width of $9.0 \pm 0.4$ nm along the screw segment to be $83\pm4$ mJ/m$^2$, being consist with the value estimated from the dissociation of APB-coupled super-partial dislocations that carry slip on (010).

Of importance to note here is that we only observed dislocations dissociated into the APB scheme to carry slip on (111) and those dissociated into the SISF scheme have never been observed.
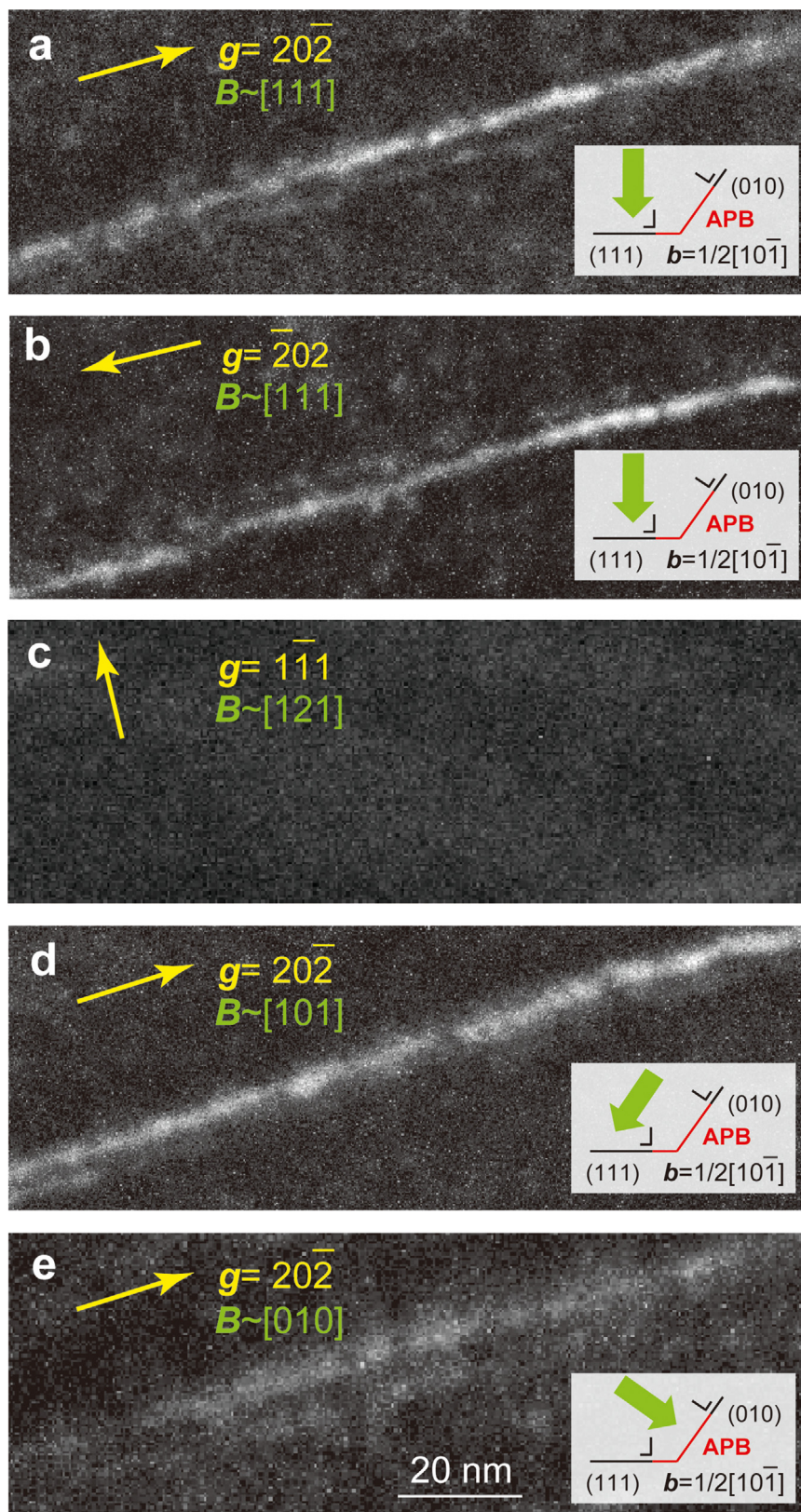
**Fig. 7.** Weak-beam dark-field TEM contrast analysis of the framed area in Fig. 6. The reflection vector **g** and electron beam incident direction **B** are indicated in each of the images.

**Table 1**

Schmid factors for slip on (111) and (010) and N-factors for each loading-axis orientation. .

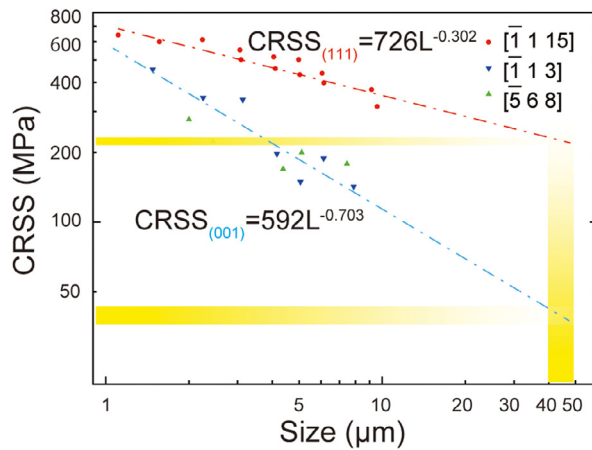| Loading-axis orientation | | $[\bar{1}, 1, 15]$ | $[\bar{1}13]$ | $[\bar{5}68]$ |
|---|---|---|---|---|
| Schmid factor | (111) $[10\bar{1}]$ | 0.433 | 0.447 | 0.383 |
| | (010) $[10\bar{1}]$ | 0.093 | 0.386 | 0.499 |
| N-factor: (010) $[10\bar{1}]$ /(111) $[10\bar{1}]$ | | 0.216 | 0.865 | 1.301 |



**Fig. 8.** Specimen size dependence of CRSS for slip on (010) ($[\bar{1}13]$- and $[\bar{5}68]$-orientated crystals) and (111) ($[\bar{1}, 1, 15]$-orientated crystals).

## 4. Discussion

### 4.1. Orientation and size dependence of CRSS for slip on (111) and (010)

Since (010)$[10\bar{1}]$ and (111)$[10\bar{1}]$ slip systems are identified respectively for the $[\bar{1}13]$ and $[\bar{5}68]$ orientations and the $[\bar{1}, 1, 15]$ orientation, CRSS values can be calculated with yield stress values defined as the stress at which the first strain burst occurs and the corresponding Schmid factors (Table 1). The CRSSs thus calculated for the (010)$[10\bar{1}]$ and (111)$[10\bar{1}]$ slip systems are plotted in Fig. 8 as a function of the specimen size (edge length $L$). The CRSS values for both the two slip systems follow an inverse power-law relationship with the specimen size $L$, i.e. $\tau_{CRSS} \propto L^{-n}$, where $n$ is a power-law exponent. For the (010)$[10\bar{1}]$ slip system, the CRSS values and their size dependence for $[\bar{1}13]$ and $[\bar{5}68]$ orientations are very similar, indicating that there is no significant orientation dependence for the operation of the (010)$[10\bar{1}]$ slip system. The $n$ values estimated for the (010)$[10\bar{1}]$ slip system is 0.703, which is comparable to those reported for FCC alloys (0.5~1.0) [18,19,21,33] and other L1$_2$ compounds such as Ni$_3$Al [18,30,34] and Co$_3$(Al,W) [20]. According to previous studies on micropillar deformation for L1$_2$ compounds such as Ni$_3$Al [18] and Co$_3$(Al,W) [20], the CRSS values extrapolated from the power-law curves of micropillar specimens of these compounds coincide with those obtained by mechanical tests of the corresponding bulk-sized single crystals when the size of micropillar specimens is in the range of 40~50 $\mu$m [18,20]. Based on this, we can deduce the bulk CRSS values for the (010)$[10\bar{1}]$ slip system in Fe$_3$Ge to be ~40 MPa (38~44 MPa). The estimated CRSS value for the (010)$[10\bar{1}]$ slip system is considerably smaller than those expected from the bulk polycrystalline yield stress obtained by Balk et al. [13], Suzuki et al. (540 MPa) [17], Ngan et al. (720 MPa) [15] and Taniguchi et al. (800 MPa) [32], even when the upper limit value (~4.7) of Taylor factor is used in the comparison. We suspect that this is due to the fact that the number of independent slip systems for the (010)$[10\bar{1}]$ slip system

is not sufficient for general deformation of polycrystalline materials.

The specimen size dependence of CRSS observed for the (111)$[10\bar{1}]$ slip system is less significant than that for the (010)$[10\bar{1}]$ slip system (Fig. 8). The $n$ values estimated for the (111)$[10\bar{1}]$ slip system is 0.302, which is in the range (0.2~0.5) often observed in BCC metals [19,28,35]. In a similar way, we can deduce the bulk CRSS values for the (111)$[10\bar{1}]$ slip system in Fe$_3$Ge to be ~240 MPa (235~250 MPa), which is by far higher than those reported for the same slip system in Ni$_3$Al (25 MPa) [3,4,20,34] or Co$_3$(Al,W) (38 MPa) [20] at room temperature. Of interest to note is that this particularly high CRSS value for the (111)$[10\bar{1}]$ slip system in Fe$_3$Ge is almost on the same magnitude as that (~320 MPa) at the peak temperature of the yield stress anomaly in Ni$_3$Al [3,4]. The less significant size dependence of CRSS for the (111)$[10\bar{1}]$ slip system is considered to be due simply to the much higher CRSS value (frictional stress), as frequently discussed in studies on micropillar deformation [35-39].

In Fe$_3$Ge, the CRSS value for the (111)$[10\bar{1}]$ slip system is an order of magnitude higher than that for the (010)$[10\bar{1}]$ slip system at room temperature. This is unusual for many other L1$_2$ compounds such as Ni$_3$Al and Co$_3$(Al,W), in which the CRSS value for the (111)$[10\bar{1}]$ slip system is by far lower than that for the (010)$[10\bar{1}]$ slip system at room temperature [3,4,40]. The only exceptional L1$_2$ compound so far identified is Pt$_3$Al [11,12] in which the (010)$[10\bar{1}]$ slip system exhibits the lower CRSS value than the (111)$[10\bar{1}]$ slip system at room temperature. However, the CRSS ratio for these two slip system for Pt$_3$Al is only 2~2.5, which is by far smaller than that (~5.8) observed in Fe$_3$Ge in the present study. This accounts for the facts the operation of the (111)$[10\bar{1}]$ slip system, the most common slip system in many other L1$_2$ compounds, is limited only in a narrow orientation range close to [001] in Fe$_3$Ge and that Fe$_3$Ge polycrystals are brittle due to the insufficient number of independent slip systems for general plasticity carried by the (010)$[10\bar{1}]$ slip system alone.

### 4.2. Factors controlling the occurrence of either (010) slip or (111) slip

Although the APB instability on (111) has been claimed to the main cause for the absence of slip on (111) in Fe$_3$Ge [7-9], slip on (111) is proved to occur in a limited orientation range close to [001] by the motion of superlattice dislocations dissociated into the APB scheme but not into the SISF scheme. The APB energy on (111) experimentally deduced in the present study is 99±9 mJ/m$^2$, which is considerably smaller than those 330 mJ/m$^2$ [9] and 320–380 mJ/m$^2$ [7] theoretically calculated. The reason for this significant difference is not known yet.

In view of the fact that the CRSS for the (111)$[10\bar{1}]$ slip system is much higher than that for the (010)$[10\bar{1}]$ slip system and that both slips occur by the motion of superlattice dislocations dissociated into the APB scheme, the plastic deformation behaviors of Fe$_3$Al and Pt$_3$Al [11,12] are identical with each other and factors controlling the occurrence of either (010) slip or (111) slip can be considered in the same line. We have proposed based on the results of core structure calculation by Vitek and Paidar [41] that because of the high energy of the CSF (complex stacking fault) in Pt$_3$Al, the core of superpartials with $\boldsymbol{b}$ = 1/2<110> bounding an APB on (111) is no-planar (spreading onto two different octahedral {111} planes along the screw orientation) (Fig. 9(a)) while it is planar when bounding an APB on (010) (Fig. 9(b)), so that the Peierls stress for the motion of APB-coupled dislocations (the CRSS value for slip on (111)) is much higher than that for slip on (001) [11,12]. This is exactly opposite to what is observed in many typical L1$_2$ compounds such as Ni$_3$Al (Figs. 9(d) and (e)). As discussed in the previous section, the CRSS ratio (5.8) for these two slip sys-
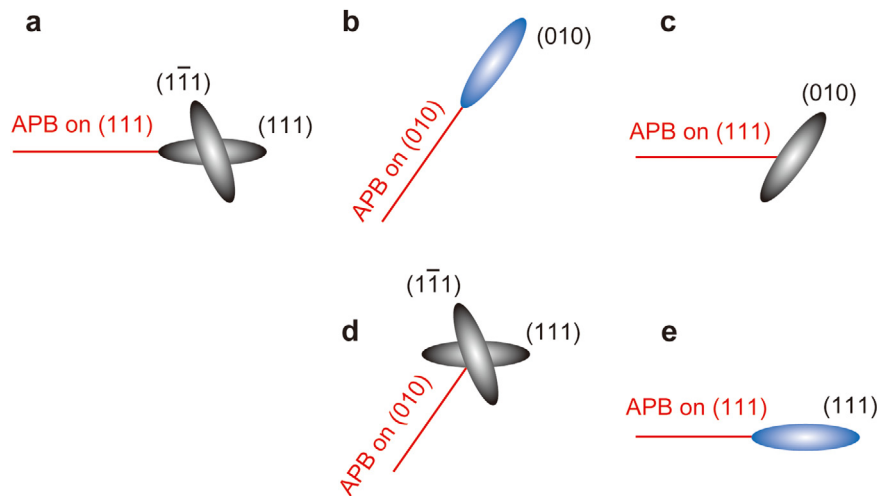
**Fig. 9.** Schematic illustrations of the core structure of the 1/2[$\bar{1}$01] APB-coupled superpartial dislocation. (a) Non-planar core structure of the 1/2[$\bar{1}$01] superpartial dislocation bounding the APB on the (111) plane (observed in Pt₃Al with a high CSF energy). (b,c) Planar and non-planar core structures of the 1/2[$\bar{1}$01] superpartial dislocation bounding the APB on the (010) and (111) planes, respectively (proposed in the present study of Fe₃Ge with a high CSF energy). (d,e) Non-planar and planar core structures of the 1/2[$\bar{1}$01] superpartial dislocation bounding the APB on the (010) and (111) planes, respectively (when the CSF energy is relatively low).

tems for Fe₃Ge is much larger than that (2~2.5) for Pt₃Al. If the CRSS ratio is reflected in how significantly the core spreading occurs, we may suspect that the core spreading for the superpartial with $b = 1/2<110>$ bounding an APB on (111) is much more significant in Fe₃Ge than in Pt₃Al (Figs. 9(b) and (c)) and that this may arise from a much higher CSF energy in Fe₃Ge. This is consistent with the high CSF energy (315 mJ/m²) as well as the narrow core spreading for the CSF dissociation calculated by Mryasov et al. [9] according to the two-dimensional Peierls-Nabarro model.

Then, one of the expected mechanical properties of Fe₃Ge is the orientation independent CRSS for slip on (010) due to the planarity of the dislocation core (Fig. 9(b)). This is indeed observed in the present micropillar compression experiments for [$\bar{1}$13]- and [$\bar{5}$68]-oriented crystals (Fig. 8). Indeed, superlattice dislocations with $b=[10\bar{1}]$ do not have any preferred orientation to align on (010) (Fig. 4). Another expected mechanical property of Fe₃Ge is the high CRSS value for slip on (111) and the preferential alignment of superlattice dislocations with $b=[10\bar{1}]$ along their screw orientation, due to the non-planar core structure of the superpartial dislocation with $b = 1/2[10\bar{1}]$ on (111). This is indeed observed in the present study, although there is another reason for the alignment of superlattice dislocations along their screw orientation (i.e., the formation of Kear-Wilsdolf locks), as will be discussed in the next section.

### 4.3. Expected temperature dependence of CRSS for slip on (010) and (111)

Any strong temperature dependence of CRSS is not expected to occur for slip on (010), since the core of the superpartial dislocation with $b = 1/2[10\bar{1}]$ on (010) is expected to be planar. This is inconsistent with the rather strong temperature dependence of yield stress previously observed for polycrystals where slip on {010} operates exclusively [13,15,17]. We believe that the strong temperature dependence of yield stress for polycrystals of Fe₃Ge originates from solid-solution hardening due to the off-stoichiometry of the compound. The incorporation of the secondary phase, η-Fe₂Ge is inevitably observed when specimens are prepared nominally at the stoichiometric composition (Fe-25 at.%Ge).

Slip on (111) is carried by the motion of superlattice dislocations dissociated into the APB scheme, in contrast to the expectation from the APB instability on {111}. These dislocations are
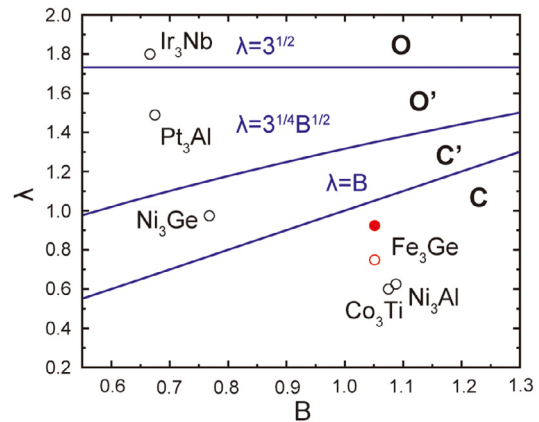


**Fig. 10.** The λ-B map proposed by Paxton et al. [42] to show the necessary condition for the yield stress anomaly to occur. The data points plotted with open symbols for Ir₃Nb, Pt₃Al, Ni₃Ge, Fe₃Ge, Ni₃Al and Co₃Ti are taken from literature [12,42,43], while the plot with the closed symbols for Fe₃Ge is from the present study. .

observed to form Kear-Wilsdorf locks through thermally-activated cross slip. This is a clear indication that Fe₃Ge exhibits yield stress anomaly when slip on (111) is activated, since the formation of Kear-Wilsdorf locks is a characteristic feature usually observed in many L1₂ compounds in the temperature region where YSA is observed. The Paxton plot [42] is often used to predict the occurrence of YSA in L1₂ compounds, in which the APB energy asymmetry and elastic torque force acting on paired superpartials are plotted as the driving forces to promote cube cross-slip to form Kear-Wilsdorf locks. Once this is done with our experimental APB energies on (111) and (010) together with the elastic constants determined by Balk et al. [13], Fe₃Ge is successfully predicted to exhibit YSA (Fig. 10), being consistent with the present study. This is based on the assumption that the relative ease of APB- and SISF-involved slip on {111} remains unchanged at high temperatures in Fe₃Ge, although SISF-involved slip on {111} is claimed to occur easily at high temperatures [15]. Although the deformation behaviors of Fe₃Ge and Pt₃Al are similar to each other in terms of the occurrence of slip on (001) and (111) and their relative ease in occurrence, the temperature dependence of CRSS for slip on (111) must

be quite different because of the difference in the driving forces for cube-cross-slip (Fig. 10). Experimental proof of the occurrence of YSA in Fe$_3$Ge is currently undertaken in our group with the use of a high-temperature stage for micropillar compression tests.

As described in the previous section, the CSF energy is expected to be very high in Fe$_3$Ge, being consistent with the results of theoretical calculations by Mryasov et al. [9]. The CSF energy is considered to be directly related to the frequency of thermally-activated cube cross-slip to form Kear-Wilsdorf locks. The higher CSF energy is believed to result in the lower onset temperature of YSA because of the ease in the constriction formation. While the onset temperature for YSA in L1$_2$ compounds with a medium CSF energy (such as Ni$_3$Al) is usually believed to be around 77 K, it should be much lower in Fe$_3$Ge. If this is the case, the CRSS value for slip on (111) is very high at room temperature because it is already considerably strengthened by YSA from a very low temperature. This may be one of the reasons why the CRSS value (~240 MPa) for slip on (111) is comparable to that (~320 MPa) at the peak temperature of the yield stress anomaly in Ni$_3$Al [3,4]. The CRSS ratio for slip on (111) and (010), which is very high (5.8) at room temperature, may be reduced as the temperature is decreased, if the onset temperature for YSA is so low, expanding the orientation range for the operation for slip on (111), and hence improving the deformability of polycrystals. On the other hand, the improvement of deformability is not expected at higher temperatures (at least, up to the peak temperature for YSA) because of the CRSS ratio is expected to be larger.

## 5. Conclusions

(1) Slip on (111) is observed for the first time to be operative at room temperature in a narrow orientation range close to [001]. The CRSS value for the (111)[10$\bar{1}$] slip system at room temperature is estimated by extrapolating the size dependent CRSS in micropillar compression to the bulk size (40~50 mm) to be ~240 MPa.

(2) Slip on (111) is carried by the motion of superlattice dislocations with **b**=[10$\bar{1}$] dissociated into the APB scheme, in contrast to the expectation from the instability of APB on (111) as previously proposed. These APB-coupled superpartials dislocations tend to align along their screw orientation forming Kear-Wilsdorf locks, a characteristic dislocation structure in many L1$_2$ compounds in the YSA temperature range.

(3) Slip on (010) is observed in other orientations with a much lower CRSS value (~40 MPa) estimated similarly. The CRSS value for slip on (010) seems not to depend much on crystal orientation. Slip on (010) is carried also by the motion of superlattice dislocations with **b**=[10$\bar{1}$] dissociated into the APB scheme. They are observed to lie on (010) without any preferred orientations, being consistent with the low Peierls stress.

(4) The APB energies on (111) and (010) are estimated from the corresponding dislocation dissociation width to be 99±9 and 91±12 mJ/m$^2$, respectively. The occurrence of yield stress anomaly for slip on (111) is predicted with these APB values and calculated elastic constants.

## Declaration of Competing Interest

None.

## Acknowledgments

## References

[1] R.C. Reed, The Superalloys, Cambridge University Press, Cambridge, 2006.

[2] J.R. Davis, Nickel, cobalt, and Their Alloys, ASM international, 2000.

[3] G.Saada.P. Veyssiere, Dislocations in Solids 10 (1996) 253–441.

[4] D.P. Pope, V. Vitek, J.L. Bassani, Dislocations in Solids 10 (1996) 135–185.

[5] D.M. Wee, O. Noguchi, Y. Oya, T. Suzuki, New L12 ordered alloys having the positive temperature dependence of strength, Trans. Jpn. Inst. Metals 21 (4) (1980) 237–247.

[6] D.M. Wee, T. Suzuki, The Temperature Dependence of Hardness of Ll2 Ordered Alloys, Trans. Jpn. Inst. Metals 20 (11) (1979) 634–646.

[7] J.B. Liu, D.D. Johnson, A.V. Smirnov, *Predicting yield-stress anomalies in L12 alloys: ni3Ge–Fe3Ge pseudo-binaries*, Acta Mater. 53 (13) (2005) 3601–3612.

[8] A.H.W. Ngan, I.P. Jones, R.E. Smallman, The stability of antiphase boundaries on {111} planes in the L12 compound Fe3Ge and its relation to the abnormal negative temperature dependence of yield strength, Philos. Mag. A 66 (1) (1992) 55–72.

[9] O.N. Mryasov, Y.N. Gornostyrev, M.V. Schilfgaarde, A.J. Freeman, *Superdislocation core structure in L12 Ni3Al, Ni3Ge and Fe3Ge: peierls–Nabarro analysis starting from ab-initio GSF energetics calculations*, Acta Mater. 50 (2002) 4545–4554.

[10] F.E. Heredia, G. Tichy, D.P. Pope, V. Vitek, Temperature and orientation dependent plastic flow in Pt3Al, Acta Metall. 37 (1989) 2755–2756.

[11] N.L. Okamoto, H. Yoshihiko, W. Hashimoto, H. Inui, Plastic deformation of single crystals of Pt3Al with the L12 structure, Philos. Mag. 93 (1–3) (2013) 60–81.

[12] N.L. Okamoto, Y. Hasegawa, H. Inui, Plastic deformation of single crystals of Pt3Al with the L12 structure having a far Al-rich off-stoichiometric composition of Pt-29at.%Al, Philos. Mag. 94 (12) (2014) 1327–1344.

[13] T.J. Balk, M. Kumar, K.J. Hemker, Influence of Fe substitutions on the deformation behavior and fault energies of Ni3Ge-Fe3Ge L12 intermetallic alloys, Acta Mater. 49 (2001) (2001) 1725–1736.

[14] A.H.W. Ngan, I.P. Jones, R.E. Smallman, On the abnormal negative temperature dependence of yield strength in the L12 compound Fe3Ge, Philos. Mag. A 65 (4) (1992) 1003–1020.

[15] A.H.W. Ngan, I.P. Jones, R.E. Smallman, *the negative temperature dependence of yield strength in the* L1$_2$ *compound* Fe$_3$Ge, Mater. Sci. Eng.: A 153 (1992) 387–391.

[16] V.A. Starenchenko, E.V. Kozlov, Y.V. Solov'eva, Y.A. Abzaev, N.A. Koneva, Orientation dependence of the yield stress and work-hardening rate of Ni3Ge at different temperatures, Mater. Sci. Eng.: A 483-484 (2008) 602–606.

[17] T. Suzuki, Y. Oya, Transition from positive to negative temperature dependence of the strength in Ni3Ge Fe3Ge solid solution, Acta Metall. 28 (1980) 301–310.

[18] M.D. Uchic, D.M. Dimiduk, J.N. Florando, W.D. Nix, Sample dimensions influence strength and crystal plasticity, Science 305 (2004) 986–989.

[19] M.D. Uchic, P.A. Shade, D.M. Dimiduk, Plasticity of Micrometer-Scale Single Crystals in Compression, Annu. Rev. Mater. Res. 39 (1) (2009) 361–386.

[20] Z.M. Chen, N.L. Okamoto, M. Demura, H. Inui, Micropillar compression deformation of single crystals of Co3(Al,W) with the L12 structure, Scr. Mater. 121 (2016) 28–31.

[21] N.L. Okamoto, S. Fujimoto, Y. Kambara, M. Kawamura, Z.M. Chen, H. Matsunoshita, K. Tanaka, H. Inui, E.P. George, Size effect, critical resolved shear stress, stacking fault energy, and solid solution strengthening in the CrMnFeCoNi high-entropy alloy, Sci. Rep. 6 (2016) 35863.

[22] Y. Hashizume, M. Inomoto, N.L. Okamoto, H. Inui, Plastic deformation of single crystals of the δ1p and δ1k intermetallic compounds in the Fe–Zn system by micropillar compression, Int. J. Plast. (2021) 136.

[23] K. Kishida, Y. Shinkai, H. Inui, Room temperature deformation of 6H–SiC single crystals investigated by micropillar compression, Acta Mater. 187 (2020) 19–28.

[24] K. Kishida, J.G. Kim, T. Nagae, H. Inui, Experimental evaluation of critical resolved shear stress for the first-order pyramidal c + a slip in commercially pure Ti by micropillar compression method, Acta Mater. 196 (2020) 168–174.

[25] Y. Hashizume, M. Inomoto, N.L. Okamoto, H. Takebayashi, H. Inui, Micropillar compression deformation of single crystals of the intermetallic compound Γ-Fe4Zn9, Acta Mater. 199 (2020) 514–522.

[26] K. Kishida, T. Maruyama, H. Matsunoshita, T. Fukuyama, H. Inui, Micropillar compression deformation of single crystals of Mo5SiB2 with the tetragonal D8l structure, Acta Mater. 159 (2018) 416–428.

[27] M. Higashi, S. Momono, K. Kishida, N.L. Okamoto, H. Inui, Anisotropic plastic deformation of single crystals of the MAX phase compound Ti3SiC2 investigated by micropillar compression, Acta Mater. 161 (2018) 161–170.

[28] J. Zhang, K. Kishida, H. Inui, Specimen size and shape dependent yield strength in micropillar compression deformation of Mo single crystals, Int. J. Plast. 92 (2017) 45–56.

[29] N.L. Okamoto, M. Inomoto, H. Adachi, H. Takebayashi, H. Inui, Micropillar compression deformation of single crystals of the intermetallic compound ζ-FeZn13, Acta Mater. 65 (2014) 229–239.

[30] K. Arora, K. Kishida, K. Tanaka, H. Inui, Effects of lattice misfit on plastic deformation behavior of single-crystalline micropillars of Ni-based superalloys, Acta Mater. 138 (2017) 119–130.

[31] Q.Z. Chen, A.H.W. Ngan, B.J. Duggan, The L12 – D019 transformation in the intermetallic compound Fe3Ge, J. Mater. Sci. Technol. 33 (1998) 5405–5414.

[32] M. Taniguchi, K. Morizumi, S. Miyazaki, S. Kumai, A. Sato, Dislocation motion on octahedral and cube planesin Fe3Ge polycrystals, Philos. Mag. 86 (10) (2006) 1327–1354.

[33] D.M. Dimiduk, M.D. Uchic, T.A. Parthasarathy, Size-affected single-slip behavior of pure nickel microcrystals, Acta Mater. 53 (15) (2005) 4065–4077.

[34] D.M. Dimiduk, M.D. Uchic, S.I. Rao, P.A. Shade, C. Woodward, G.B. Viswanathan, E.M. Nadgorny, S. Polasik, D.M. Norfleet, M.J. Mills, Strengthening and plastic flow of Ni3Al alloy microcrystals, Philos. Mag. 93 (1–3) (2013) 96–120.

[35] S.W. Lee, W.D. Nix, Size dependence of the yield strength of fcc and bcc metallic micropillars with diameters of a few micrometers, Philos. Mag. 92 (10) (2012) 1238–1260.

[36] M.D. Uchic, D.M. Dimiduk, A methodology to investigate size scale effects in crystalline plasticity using uniaxial compression testing, Mater. Sci. Eng.: A 400-401 (2005) 268–278.

[37] R. Soler, J.M. Wheeler, H.J. Chang, J. Segurado, J. Michler, J. Llorca, J.M. Molina-Aldareguia, Understanding size effects on the strength of single crystals through high-temperature micropillar compression, Acta Mater. 81 (2014) 50–57.

[38] J.R. Greer, J.T.M. De Hosson, *Plasticity in small-sized metallic systems: intrinsic versus extrinsic size effect*, Prog. Mater. Sci. 56 (6) (2011) 654–724.

[39] E. Bittencourt, Interpretation of the size effects in micropillar compression by a strain gradient crystal plasticity theory, Int. J. Plast. 116 (2019) 280–296.

[40] A. Suzuki, H. Inui, T.M. Pollock, L1$_2$-Strengthened *Cobalt-Base Superalloys*, Annu. Rev. Mater. Res. 45 (1) (2015) 345–368.

[41] V. Paidar, D.P. Ppoe, V. Vitek, A theory of the anomalous yield behavior in Ll2 ordered alloys, Acta Metall. 32 (1984) 435–448.

[42] A.T. Paxton, Y.Q. Sun, The role of planar fault energy in the yield anomaly in L12 intermetallics, Philos. Mag. A 78 (1) (1998) 85–104.

[43] N.L. Okamoto, S. Takemoto, Z.M. Chen, M. Yamaguchi, H. Inui, FCC metal-like deformation behaviour of Ir3Nb with the L12 structure, Int. J. Plast. 97 (2017) 145–158.